Electronic Supplementary Information

Influence of Interfacial Tensile Strain on Charge Transport Characteristics of MoS$_2$-based Vertical Heterojunction Devices

Fu Huang,[†ab] Byungjin Cho,[†c] Hee-Suk Chung,[a] Seung Bae Son,[a] Jung Han Kim,[ad] Tae-Sung Bae,[a] Hyung Joong Yun,[e] Jung Inn Sohn,[f] Kyu Hwan Oh,[d] Myung Gwan Hahm,[g] Jung Hee Park,[b] and Woong-Ki Hong[a]*

[a]Jeonju Center, Korea Basic Sicence Intstitute, Jeonju, Jeollabuk-do 54907, Republic of Korea;

[b]Division of Biotechnology, Advanced Institute of Environment and Bioscience, College of Environmental and Bioscience Sciences, Chonbuk National University, Iksan 54596, Republic of Korea

[c]Department of Advanced Functional Thin Films, Surface Technology Division, Korea Institute of Materials Science, Changwon, Gyeongnam 51508, Republic of Korea

[d]Department of Materials Science and Engineering, Seoul National University, Seoul 08826, Republic of Korea

[e]Advanced Nano Surface Research Group, Korea Basic Science Institute, Daejeon 34133, Republic of Korea

[f]Department of Engineering Science, University of Oxford, Oxford OX1 3PJ, UK

[g]School of Materials Science and Engineering, Inha University, Incheon 22212, Republic of Korea

[†]These authors equally contributed to this work.

*Corresponding author: E-mail: (W.-K.H) wkh27@kbsi.re.kr

Table of Contents

1. Strain calculation in MoS$_2$ directly grown on a p-Si substrate

Figure S1a and b display the statistical frequency distribution between the E$^1_{2g}$ and A$_{1g}$ modes for the A-MoS$_2$ and T-MoS$_2$ films on a p-Si substrate, respectively. Figure S1c shows the frequency difference (A$_{1g}$ - E$^1_{2g}$) between the A-MoS$_2$ and T-MoS$_2$ films. In Figure S1a,b, the differences between the E$^1_{2g}$ and A$_{1g}$ modes are 23.4 and 21.4 cm^{-1} for the A-MoS$_2$ and T-MoS$_2$ films, respectively. As shown in Figure S1c, the A$_{1g}$ peak of the A-MoS$_2$ shows a negligible redshift of ~0.1 cm^{-1}, whereas the E$^1_{2g}$ peak of the A-MoS$_2$ shows a significant redshift of ~2.0 cm^{-1} compared to those of the T-MoS$_2$. Using the Gruneisen parameter of the E$^1_{2g}$ mode for MoS$_2$,[1-4] we can calculate the biaxial lattice strain in the A- MoS$_2$ by applying the following equation[1]:

$$\varepsilon = \frac{\omega - \omega_0}{2\gamma\omega_0} = \frac{382.75 - 384.74}{2 * 0.65 * 384.74} = -0.398\%$$

where ω and ω_0 are the Raman wave number at finite strain and zero strain, respectively, γ is the Gruneisen parameter of E$^1_{2g}$ (0.65),[2] and ε is the biaxial strain.
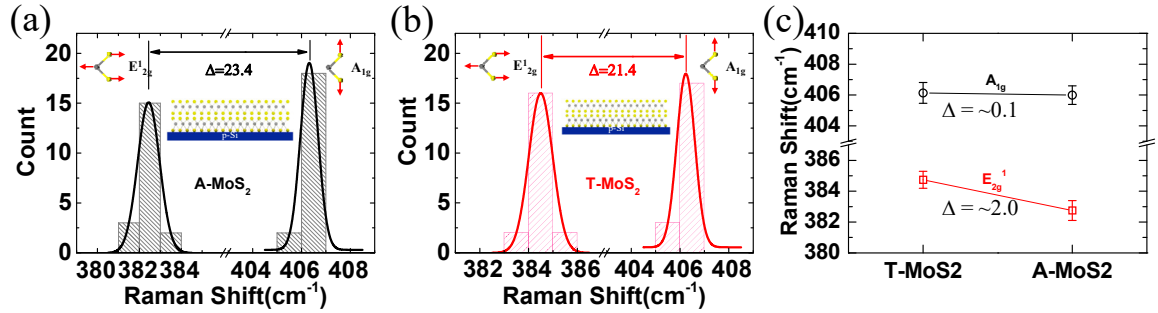
Figure S1. The statistical frequency distribution of the E$^1_{2g}$ and A$_{1g}$ modes for the (a) A-MoS$_2$ and (b) T-MoS$_2$ films on the p-Si substrate. (c) The frequency difference between the A-MoS$_2$ and T-MoS$_2$ films for the E$^1_{2g}$ and A$_{1g}$ modes.

2. TEM data for the A-MoS$_2$ and T-MoS$_2$ samples
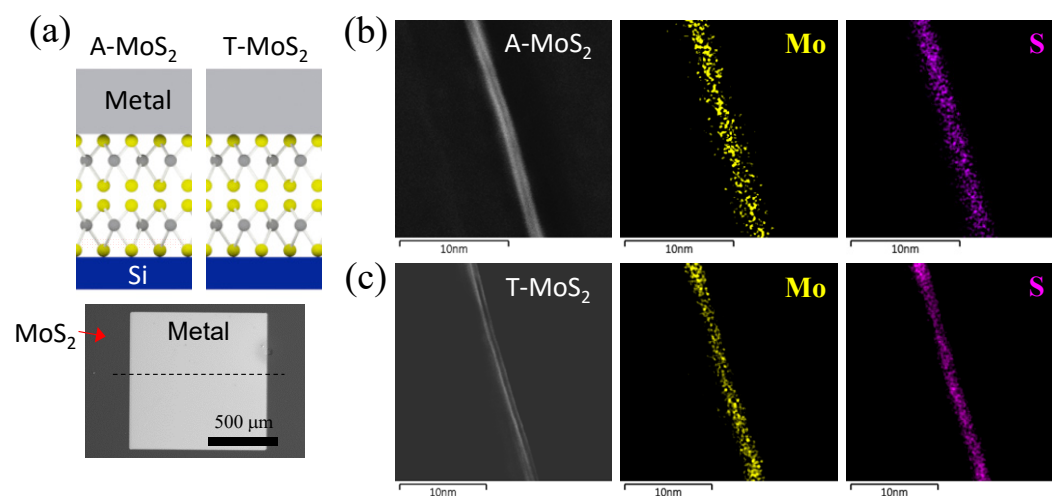
Figure S2. (a) Schematic illustration (upper panel) and a representative plan-view SEM image (lower panel) showing the cross-section for the A-MoS$_2$ and T-MoS$_2$ samples. (b) STEM image and corresponding EDX results for the A-MoS$_2$ and T-MoS$_2$ samples.

3. XPS data comparison between previous reports and our work for binding energy of the Mo 3d and S 2p peaks

The binding energy of the Mo 3d and S 2p core levels in MoS_2 obtained from XPS is summarized in Table S1.

Table S1. XPS data comparison for binding energy of the Mo 3d and S 2p peaks

| Number	Binding Energy (eV)				References	
	Mo 3d $_{3/2}$	Mo 3d $_{5/2}$	S 2p $_{1/2}$	S 2p $_{3/2}$		
1	232.4	229.2	163.1	162.2	[5]	
2	232.4	229.4	163.3	162.2	[6]	
3	232.5	229.3	163.3	162.2	[7]	
4	232.6	229.4	163.3	162.2	[8]	
5	232.5	229.3	163.3	162.1	[9]	
6	232.3	229.2	163.3	162	[10]	
7	-	229	-	162	[11]	
8	232.4	229.2	163.3	162.1	[12]	
9	232.5	229.3	163.3	162.2	[13]	
10	232	228.8	163.3	162	[14]	
11	232	229	163	161.8	[15]	
12	232.4	229.1	163	162.2	[16]	
13	231.9	228.7	162.7	161.5	[17]	
14	-	229	-	161.8	[18]	
15	232.6	229.4	163.3	162.3	[19]	
16	232.1	228.9	163.1	162.1	[20]	
17	233	230	164	163	[21]	
18	233	230	-	-	[22]	
19	**232.4**	**229.2**	**163.3**	**162.1**	**T-MoS$_2$**	**Our Works**
	233.1	**229.9**	**163.8**	**162.7**	**A-MoS$_2$**	

4. Work function comparison of MoS_2 films between previous reports and our work

We examined ultraviolet photoemission spectroscopy (UPS) to study the electronic structures of the A-MoS_2 and T-MoS_2 films. From the UPS measurement, the WF was calculated from the difference between the secondary electron cut-off of the highest binding energy (Figure 3a) and the exciting photon energy of 21.22 eV. The valence band maximum (VBM) was determined from the cut-off of the lowest binding energy (Figure 3b). The work function (WF) values from previous reports and our work are summarized in Table S2.

Table S2. Work function values of MoS_2 from previous reports and our work.

	Photon source energy (eV)	Secondary electron edge (eV)	WF (eV)	VBM (eV)	References
T-MoS$_2$	**21.22**	**17.02**	**4.2**	**1.43**	**Our work**
A-MoS$_2$		**16.97**	**4.25**	**1.3**	
Pristine MoS$_2$		16.84	4.36		
150 ℃ MoS$_2$	21.2	16.68	4.52	-	[23]
250 ℃ MoS$_2$		16.68	4.52		
80℃ MoS$_2$	21.22	16.81	4.41	0.69	[24]
200 ℃ MoS$_2$		16.70	4.52		
MoS$_2$	21.2	16.01	5.19	-	[25]
ce-MoS$_2$	-	-	4.50	-	[26]
O-ce-MoS$_2$	-	-	4.93	-	
n-MoS$_2$	21.2	17	4.2	1.7	[27]
Pristine MoS$_2$		16.59	4.63	1.32	
N1- MoS$_2$	21.22	17.65	3.57	1.76	[28]
P1 - MoS$_2$		15.74	5.48	1.06	

5. Band-gap modulation under biaxial tensile strain for the A-MoS₂ bilayer

The electron affinity (χ) and energy gap (E_g) of p-Si are ~4.05 and ~1.1 eV, respectively.[29,30] The work function (Φ) of Al is 4.3 eV[31] and the electron affinity (χ) of MoS₂ is ~4.1 eV.[32,33] Meanwhile, from UPS measurements, we found the Φ of ~4.25 and ~4.2 eV for the A-MoS₂ and T-MoS₂, respectively. Here, assuming that the bilayer T-MoS₂ is tensile-strain-free, the energy gap (E_g) of the A-MoS₂ and T-MoS₂ can be expressed by the following equation,

$$E_{g,MoS_2} = E_F - VBM + \Phi_{MoS_2} - \chi_{MoS_2}$$

where E_F is the Fermi level energy, VBM is the valence band maximum, Φ_{MoS2} is the work function of MoS₂, χ_{MoS2} is the electron affinity of MoS₂.

Furthermore, we can estimate the decreased rate of the energy gap under biaxial tensile strain (ΔE_g) using the following equation,

$$\Delta E_g \left({eV}/{\%} \right) = - \frac{E_{g,T-MoS_2} - E_{g,A-MoS_2}}{\varepsilon_{bi}}$$

where ε_{bi} is a biaxial lattice tensile strain for the A-MoS₂ on the p-Si substrate (~0.398%) (see Figure S1). Thus, the band-gap modulation under biaxial tensile strain for a MoS₂ bi-layer is -0. 2 eV per % strain.

6. Fabrication process of the MoS$_2$-based heterojunction devices

Figure S3 shows the fabrication process of vertical p-n heterojunction devices. First, the p-type Si wafers were cleaned using DI water, acetone, and isopropyl alcohol and then dried by the blowing of nitrogen gas (Figure S3a). After that, the MoS$_2$ films are directly synthesized or transferred on the p-Si substrate (Figure S3b). Note that the transferred MoS$_2$ films were synthesized on a SiO$_2$/p-Si substrate first and then were transferred onto another p-Si substrate. Finally, top and bottom electrodes were fabricated on an MoS$_2$/p-Si substrate using a thermal evaporator (Figure S3c and d).
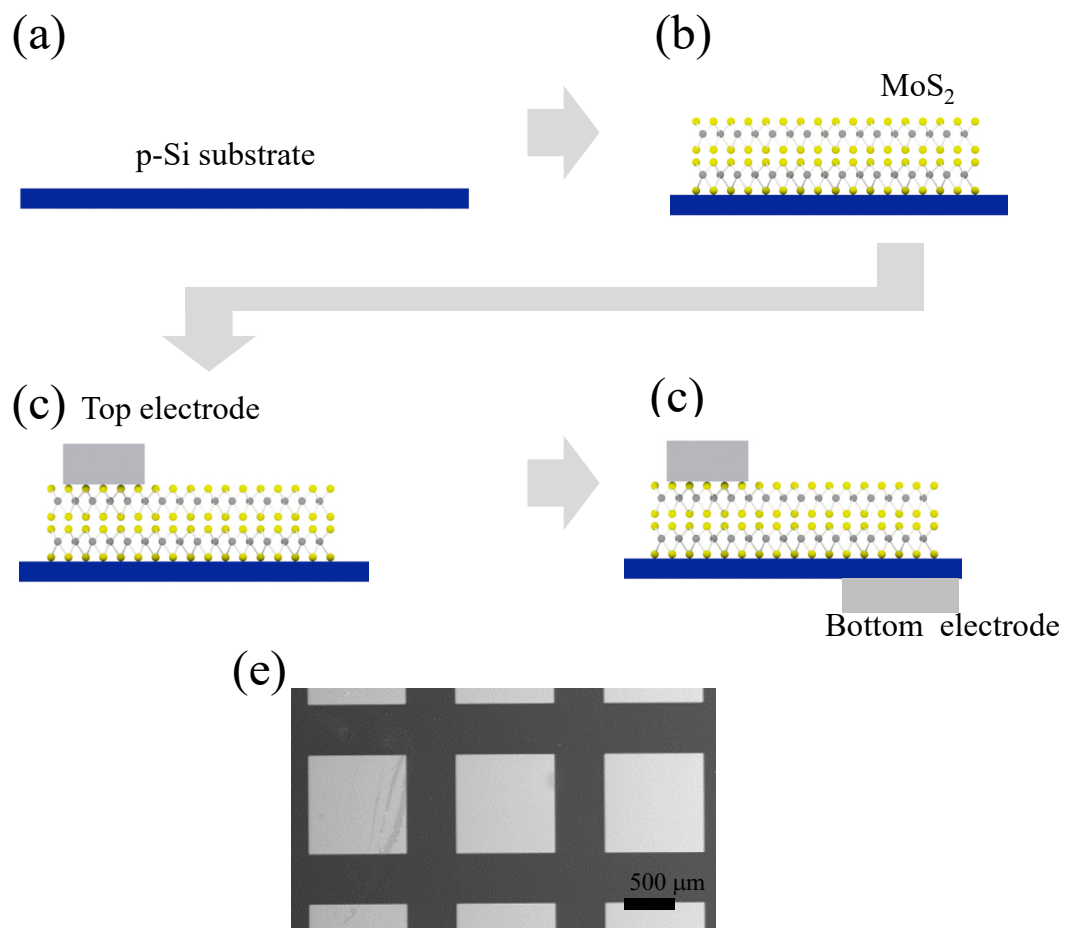
Figure S3. (a-d) Fabrication process of MoS$_2$-based heterojunction devices. (e) A representative plan-view SEM image of the fabricated vertical heterojunction devices

7. Statistical distribution of turn-on voltages and idealityfactors for the A-MoS$_2$-based and T-MoS$_2$-based heterojunction devices

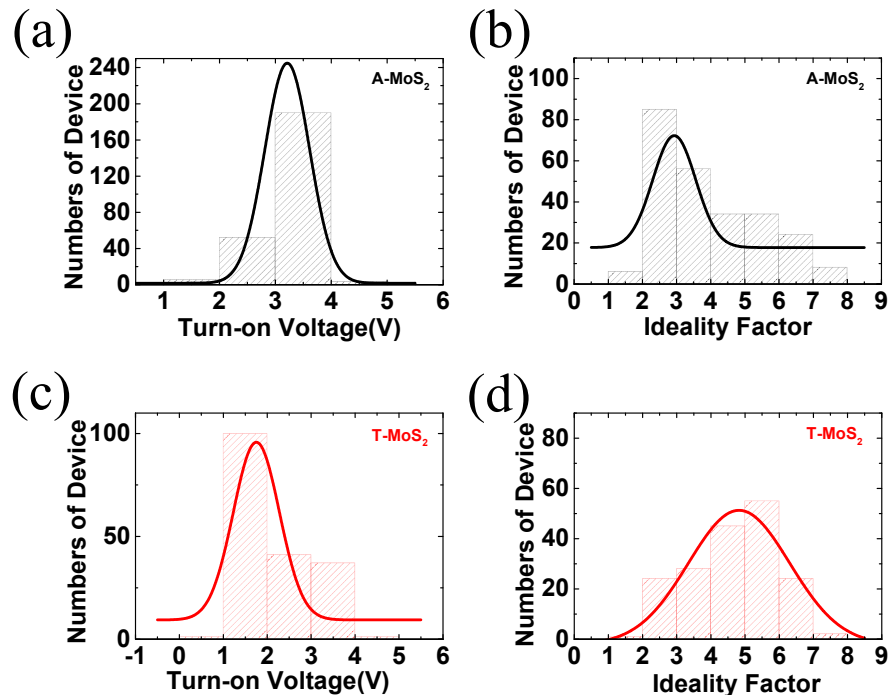
Figure S4. The statistical distribution of turn-on voltages and ideality factors for vertical heterojunction devices based on A-MoS$_2$ and T-MoS$_2$ films.

8. The photocurrent versus light power density for the A-MoS$_2$-based and T-MoS$_2$-based heterojunction devices

Figures 4d and e show the absolute current under dark/illumination at a forward and reverse voltages of 5 and -5 V from I-V curves (Figures 4b and c), respectively, for the A-MoS$_2$-based and T-MoS$_2$-based heterojunction devices. In Figure S5, the photocurrent is the difference between the current under illumination and the dark current, namely $I_{ph} = I_{light} - I_{dark}$. The absolute current and photocurrent of the A-MoS$_2$-based and T-MoS$_2$-based devices are summarized in Tables S3 and S4 below.
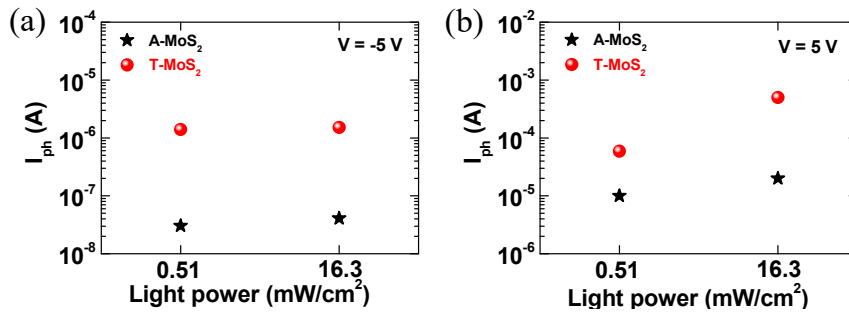

Figure S5. I_{ph} vs. light power density at (a) reverse and (b) forward bias for the A-MoS$_2$-based and T-MoS$_2$-based devices.

Table S3. Absolute current for the A-MoS$_2$-based and T-MoS$_2$-based devices.

Absolute current	Bias condition	I_{dark}	$I_{light\ (0.51)}$ at 0.51 mW/cm^2	$I_{light\ (16.3)}$ at 16.3 mW/cm^2
A-MoS$_2$	-5 V	4.30×10^{-8} A	7.34×10^{-8} A	1.44×10^{-6} A
T-MoS$_2$	-5 V	8.76×10^{-10} A	4.19×10^{-8} A	1.52×10^{-6} A
A-MoS$_2$	5 V	2.72×10^{-4} A	2.82×10^{-4} A	3.31×10^{-4} A
T-MoS$_2$	5 V	1.9×10^{-3} A	1.92×10^{-3} A	2.42×10^{-3} A

Table S4. Photocurrent for the A-MoS$_2$-based and T-MoS$_2$-based devices.

Photocurrent	Bias condition	$I_{ph\ (0.51)} = I_{light\ (0.51)} - I_{dark}$	$I_{ph\ (16.3)} = I_{light\ (16.3)} - I_{dark}$
A-MoS$_2$	-5 V	3.04×10^{-8} A	1.40×10^{-6} A
T-MoS$_2$	-5 V	4.10×10^{-8} A	1.52×10^{-6} A
A-MoS$_2$	5 V	0.1×10^{-4} A	0.59×10^{-4} A
T-MoS$_2$	5 V	0.02×10^{-3} A	0.5×10^{-3} A

9. The phoresponsivity versus light power density for the A-MoS$_2$-based and T-MoS$_2$-based heterojunction devices

Figure S6a shows a logarithm scale plot of current (y-axis) versus linear time scale (x-axis), which is the changed form of Figure 4f. The photoresponsivity, which is described as $R_{ph} = I_{ph}/P_{light}$ with light intensity P_{light}, is shown in Figure S6b below. Under light power density of 16.3 (0.51) mW/cm^2, the R_{ph} at a reverse voltage of -5 V is $\sim$ 0.34 (0.23) and $\sim$ 0.37 (0.32) A/W for the A-MoS$_2$-based and T-MoS$_2$-based device, respectively.
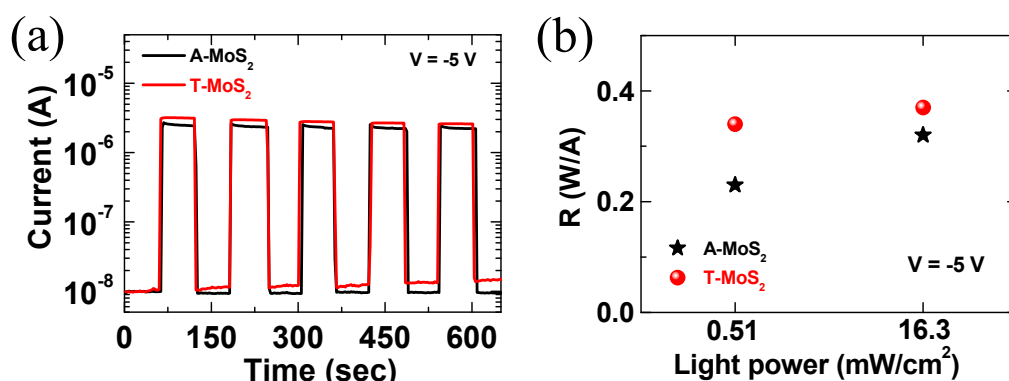

Figure S6. (a) A semi-logarithm scale plot of photoswitching curves of the A-MoS$_2$-based and T-MoS$_2$-based devices. (b) Photoresponsivity vs. light power density at -5 V for the A-MoS$_2$-based and T-MoS$_2$-based devices.

10. The photovoltaic effect of the A-MoS$_2$-based and T-MoS$_2$-based heterojunction devices
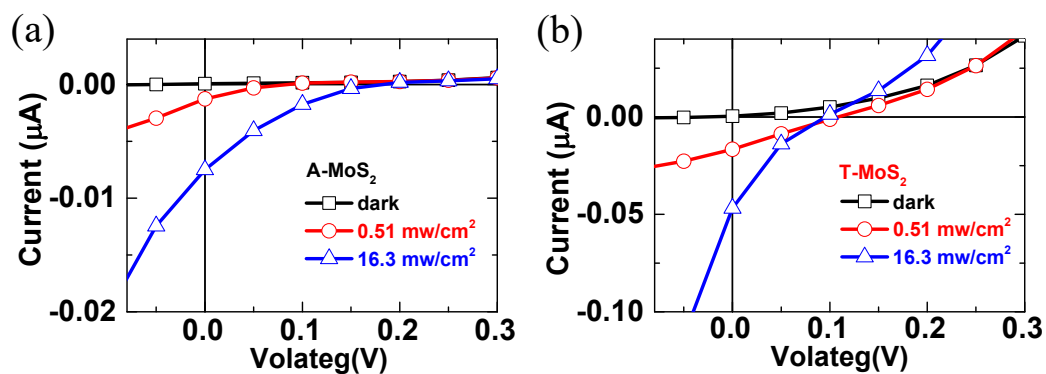
Figure S7. The current-voltage characteristics showing photovoltaic effect for the vertical heterojunction devices based on A-MoS$_2$ and T-MoS$_2$ films.

Table S5. Photovoltaic parameters of the A-MoS$_2$-based and T-MoS$_2$-based heterojunction solar cell under light power density of 16.3 mW/cm^2.

Type	V_{OC}	I_{SC}	FF
A-MoS$_2$	0.18 ± 0.03 V	20.7 ± 17.9 nA	0.12 ± 0.05
T-MoS$_2$	0.11 ± 0.02 V	104.2 ± 62.4 nA	0.17 ± 0.02

11. Correlation between the defect sites and the amount of decreasing current for two types of devices

According to Ref. [34], we tried to qualitatively calculate trap density from the dynamic curve of photoswitching although the calculation in our work is rough. From Figure R4 below, we determined the dominant time constant from the time when the signal reaches 37% of its maximum value. From the absorbed photon flux at saturation region $\phi_{sat} = \eta P_{light}\lambda/Ahc$, where $\eta \approx 0.15$ is the optical absorption of MoS$_2$ in the visible, P_{light} is the light power (4.12 μW), λ is the wave length, A is the area of illumination (2.6×10^{-4} cm^2), h is Planck's constant (6.63×10^{-34} Js), and c is the speed of light (3.0×10^8 m/s), the trap density at saturation can roughly be estimated as $N_{sat} = \phi_{sat}\tau_s$. Note that we assumed λ = 665 nm, which was a dominant peak when we measured spectrum of white-light and from Figure S8b, τ_s can be determined to 2 s and 1.5 s for the A-MoS$_2$ and T-MoS$_2$, respectively.

The calculated trap density is 16.2×10^{15} and 12.2×10^{15} cm^{-2} for the A-MoS$_2$-based and T-MoS$_2$-based devices, respectively. The trapped charge density of the T-MoS$_2$-based device is lower than that of A-MoS$_2$-based device. This can be attributed to the increase in positively charged trap sites due to thicker silicon oxide at the MoS$_2$-Si interface for the A-MoS$_2$ based device.[35-36]
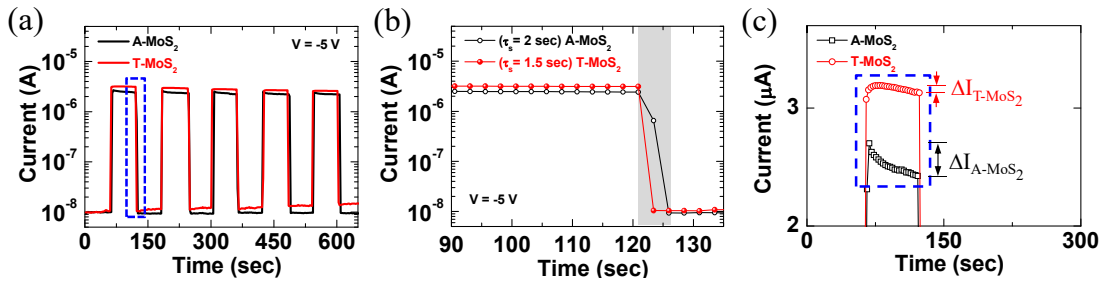
Figure S8. (a) Semi-log plot of Photoswitching curves and (b) current decay curves (zoom-in graph of blue box region in Figure S8a) of the A-MoS$_2$-based and T-MoS$_2$-based devices. (c) Linear scale photoswitching curves showing the difference of decreasing current.

Table S6. Parameters for calculation of charge trap density (τ_s: dominant time constant, ϕ_{sat}: absorbed photon flux at saturation region, and N_{sat}: trapped charge density)

Device type	τ_s	ϕ_{sat}	N_{sat}
A-MoS$_2$	2 s	8.11×10^{15} s^{-1}cm^{-2}	16.2×10^{15} cm^{-2}
T-MoS$_2$	1.5 s	8.11×10^{15} s^{-1}cm^{-2}	12.2×10^{15} cm^{-2}

12. Schematic energy band diagrams of the A-MoS$_2$ and T-MoS$_2$ under the equilibrium state and under bias conditions

As shown in Figures 3c,d, the energy band diagrams of the A-MoS$_2$-based and T-MoS$_2$-based heterojunctions were constructed based on the UPS results. Figure S9 shows schematic energy band diagrams of only the A-MoS$_2$ and T-MoS$_2$ layers under the equilibrium state and under bias conditions before and after illumination. The A-MoS$_2$ layer in our work was directly synthesized on the p-type substrate using a CVD system, whereas the T-MoS$_2$ layer was transferred onto the p-Si substrate after CVD-synthesis on an SiO$_2$ substrate to release strain by interaction between the SiO$_2$ substrate and MoS$_2$. For the A-MoS$_2$, tensile strain arising from a thermal expansion mismatch and the SiO$_2$ layer formation during the direct synthesis of MoS$_2$ on the p-Si substrate[1,4,37-40] can create charge trap states induced by disorder, defects, or S vacancies[34,41-43] and lead to a reduction of the energy band gap. Due to the charge trap states through the formation of SiO$_2$ layer, the Fermi level pinning can be caused at the interface between A-MoS$_2$ and p-Si.[44,45] Additionally, in our work, Al as a top contact electrode of vertical heterojunctions can be classified as a metal with weak adsorption (physisorption) on 2D van der Waals materials.[46,47] Accordingly, the energy band in the A-MoS$_2$ slopes downwards towards the contact of the p-Si side (the Al top contact) under forward bias (under reverse bias), as shown in Figure S6a. Under illumination, the contribution of photo-excited carriers to the modulation of the band slope can be negligible due to the Fermi level pinning and charge recombination induced by tensile strain through the formation of SiO$_2$ layer at the interface between p-Si and A-MoS$_2$. In contrast, the band slope in the T-MoS$_2$ for the p-Si/T-MoS$_2$/Al heterojunctions can switch its direction at the Al top contact or the p-Si contact, as shown in Figure S6b. The band slope of the T-MoS$_2$ under illumination can be

strongly affected by photoexcited carriers due to weakly interacting contacts at the p-Si/T-MoS$_2$/Al heterointerfaces. These energy band diagrams can be considered as the modulation of energy band slopes for vertically-stacked graphene-MoS$_2$- graphene or graphene-MoS$_2$-metal (Ti) heterojunction devices.[33,48]
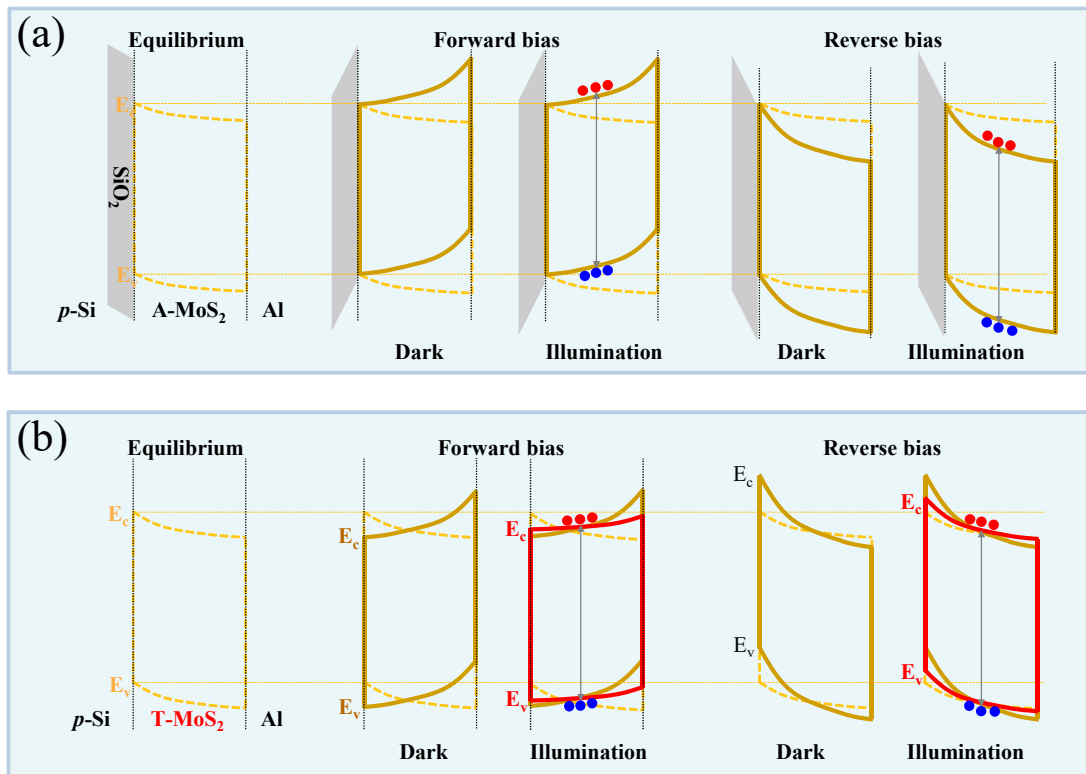

Figure S9. Schematic energy band diagrams of the A-MoS$_2$ and T-MoS$_2$ under the equilibrium state and under bias conditions before and after illumination.

13. Tunneling barrier heights under dark and light illumination for the A-MoS$_2$-based and T-MoS$_2$-based heterojunction devices

The effective values of ϕ_B under dark and light illumination for the A-MoS$_2$-based and T-MoS$_2$-based heterojunctions were estimated from the slope of the linear fits in the high forward bias region highlighted with the green colour in each figure (Figures 6a and b). The tunneling barrier heights for the A-MoS$_2$-based and T-MoS$_2$-based heterojunctions are summarized in Table S7 below.

Table S7. The barrier heights under dark and light illumination for A- MoS$_2$-based and T-MoS$_2$-based heterojunctions

	ϕ_B for A-MoS$_2$	ϕ_B for T-MoS$_2$
Dark	0.58 ± 0.27 eV	0.39 ± 0.1 eV
Illumination	0.57 ± 0.28 eV	0.35 ± 0.1 eV

References

[1] S. Wang, X. Wang, J. H. Warner, *ACS Nano* 2015, **9**, 5246.

[2] C. Rice, R. Young, R. Zan, U. Bangert, D. Wolverson, T. Georgiou, R. Jalil, K. S. Novoselov, *Phys. Rev. B* 2013, **87**, 081307.

[3] Y. Cai, J. Lan, G. Zhang, Y.-W. Zhang, *Phys. Rev. B* 2014, **89**, 035438.

[4] H. J. Conley, B. Wang, J. I. Ziegler, R. F. Haglund Jr, S. T. Pantelides, K. I. Bolotin, *Nano Lett.* 2013**, 13**, 3626.

[5] S. Hu, W. Chen, J. Zhou, F. Yin, E. Uchaker, Q. Zhang, G. Cao, *J. Mater. Chem. A* 2014, **2,** 7862.

[6] C.-J. Liu, S.-Y. Tai, S.-W. Chou, Y.-C. Yu, K.-D. Chang, S. Wang, F. S.-S. Chien, J.-Y. Lin, T.-W. Lin, *J. Mater. Chem.* 2012, **22,** 21057.

[7] S.-H. Su, W.-T. Hsu, C.-L. Hsu, C.-H. Chen, M.-H. Chiu, Y.-C. Lin, W.-H. Chang, K. Suenaga, -.H. He Jr, L.-J. Li, *Front. Energy Res.* 2014, **2,** 27.

[8] S. A. Patil, P.Y. Kalode, R. S. Mane, D. V. Shinde, A. Doyoung, C. Keumnam, M. Sung, S. B. Ambade, S.-H. Han, *Dalton Trans.* 2014, **43**, 5256.

[9] D. Gao, M. Si, J. Li, J. Zhang, Z. Zhang, Z. Yang, D. Xue, *Nanoscale Res. Lett.* 2013, **8**, 1.

[10] Y. Shi, J.-K. Huang, L. Jin, Y.-T. Hsu, S. F. Yu, L.-J. Li, H. Y. Yang, *Sci. Rep.* 2013, **3**, 1839

[11] J. Kibsgaard, Z. Chen, B. N. Reinecke, T. F. Jaramillo, *Nat. Mater.* 2012**, 11**, 963.

[12] Y. Shi, Y. Wang, J. I. Wong, A. Y. S. Tan, C.-L. Hsu, L.-J. Li, Y.-C. Lu, H. Y. Yang, *Sci. Rep.* 2013**, 3**, 2169

[13] Y. H. Lee, X. Q. Zhang, W. Zhang, M. T. Chang, C. T. Lin, K. D. Chang, Y. C. Yu, J. T. W. Wang, C. S. Chang, L. J. Li, T.-W. Lin, *Adv. Mater.* 2012**, 24**, 2320.

[14] Z. Chen, X. Liu, Y. Liu, S. Gunsel, J. Luo, *Sci. Rep.* **2015,** *5*, 12869

[15] W. Yang, Q.-Q. Sun, Y. Geng, L. Chen, P. Zhou, S.-J. Ding, D. W. Zhang, *Sci. Rep.* 2015**, 5**, 11921

[16] P. Shah, T. N. Narayanan, C.-Z. Li, S. Alwarappan, *Nanotechnol.* 2015**, 26**, 315102.

[17] J. Tao, J. Chai, L. Guan, J. Pan, S. Wang, *Appl. Phys. Lett.* 2015**, 106**, 081602.

[18] S. D. Namgung, S. Yang, K. Park, A.-J. Cho, H. Kim, J.-Y. Kwon, *Nanoscale Res. Lett.* 2015**, 10**, 1.

[19] L. Shi, L. Liang, F. Wang, M. Liu, J. Sun, *Energy Envir. Foc.* 2015**, 4**, 74.

[20] L. Cao, R. Wang, D. Wang, X. Li, H. Jia, Activity. *Mater. Lett.* 2015, **160**, 286.

[21] S. M. Tan, A. Ambrosi, Z. Sofer, Š. Huber, D. Sedmidubský, M. Pumera, *Chem. Eur. J.* 2015, **21**, 7170.

[22] H. Qiu, L. Pan, Z. Yao, J. Li, Y. Shi, X. Wang, *Appl. Phys. Lett.* 2012, **100**, 123104.

[23] J.-M. Yun, Y.-J. Noh, J.-S. Yeo, Y.-J. Go, S.-I. Na, H.-G. Jeong, J. Kim, S. Lee, S.-S. Kim, H.Y. Koo, T.-W. Kim, D.-Y. Kim, *J. Mater. Chem. C* 2013, **1**, 3777.

[24] K. Jiao, C. Duan, X. Wu, J. Chen, Y. Wang, Y. Chen, *Phys. Chem. Chem. Phys.* 2015**, 17**, 8182.

[25] P. Qin, G. Fang, W. Ke, F. Cheng, Q. Zheng, J. Wan, H. Lei, X. Zhao, *J. Mater. Chem. A* 2014, **2**, 2742.

[26] X. Yang, W. Fu, W. Liu, J. Hong, Y. Cai, C. Jin, M. Xu, H. Wang, D. Yang, H. Chen, *J. Mater. Chem. A* 2014, **2**, 7727.

[27] M.-L. Tsai, S.-H. Su, J.-K. Chang, D.-S. Tsai, C.-H. Chen, C.-I. Wu, L.-J. Li, L.-J. Chen, J.-H. He, *ACS Nano* 2014**, 8**, 8317.

[28] A. Tarasov, S. Zhang, M. Y. Tsai, P. M. Campbell, S. Graham, S. Barlow, S. R.

Marder, E. M. Vogel, *Adv. Mater.* 2015, **27**, 1175.

[29] Y. Li, C.-Y. Xu, J.-Y. Wang, L. Zhen, *Sci. Rep.* 2014, **4**, 7186

[30] C. Yim, M. O'Brien, N. McEvoy, S. Riazimehr, H. Schäfer-Eberwein, A. Bablich, R. Pawar, G. Iannaccone, C. Downing, G. Fiori, M. C. Lemme, G. S. Duesberg, *Sci. Rep.* 2014**, 4**, 5458.

[31] C. Gong, L. Colombo, R. M. Wallace, K. Cho, *Nano Lett.* 2014, **14**, 1714.

[32] H. Jeong, S. Bang, H. M. Oh, H. J. Jeong, S.-J. An, G. H. Han, H. Kim, K. K. Kim, J. C. Park, Y. H. Lee, G. Lerondel, M. S. Jeong, *ACS Nano* 2015, **9**, 10032.

[33] W. J. Yu, Z. Li, H. Zhou, Y. Chen, Y. Wang, Y. Huang, X. Duan, *Nat. Mater.* 2013, **12**, 246.

[34] M. M. Furchi, D. K. Polyushkin, A. Pospischil, T. Mueller, *Nano Lett.* 2014**, 14**, 6165.

[35] D. J. DiMaria, D. Arnold, E. Cartier, *Appl. Phys. Lett.* 1992, **60**, 2118.

[36] E. H. Snow, A. S. Grove, B. E. Deal, C. T. Sah, *J. Appl. Phys.* 1965, **36**, 1664.

[37] K. Liu, Q. Yan, M. Chen, W. Fan, Y. Sun, J. Suh, D. Fu, S. Lee, J. Zhou, S. Tongay, J. Ji, J. B. Neaton, J. Wu, *Nano Lett.* 2014, **14**, 5097.

[38] Y. Y. Hui, X. Liu, W. Jie, N. Y. Chan, J. Hao, Y.-T. Hsu, L.-J. Li, W. Guo, S. P. Lau, *ACS Nano* 2013, **7**, 7126.

[39] K.-G. Zhou, F. Withers, Y. Cao, S. Hu, G. Yu, C. Casiraghi, *ACS Nano* 2014, **8**, 9914.

[40] Z. Liu, M. Amani, S. Najmaei, Q. Xu, X. Zou, W. Zhou, T. Yu, C. Qiu, A. G. Birdwell, F. J. Crowne, R. Vajtai, B. I. Yakobson, Z. Xia, M. Dubey, P. M. Ajayan, J. Lou, *Nat. Commun.* 2014, **5**, 5246.

[41] J. Yang, Y. Zhang, W.-J. Yin, X. Gong, B. I. Yakobson, S.-H. Wei, *Nano Lett.* 2016, **16**, 1110.

[42] D. Kufer, G. Konstantatos, 2015, **15**, 7307.

[43] W. Zhu, T. Low, Y.-H. Lee, H. Wang, D. B. Farmer, J. Kong, F. Xia, P. Avouris, *Nat. Commun.* 2014, **5**, 3087.

[44] Y. Guo, D. Liu, J. Robertson, *ACS Appl. Mater. Interfaces* 2015**, 7,** 25709.

[45] S. Lee, A. Tang, S. Aloni, H.-S. Philip Wong, *Nano Lett.* 2016**, 16**, 276.

[46] C. Gong, D. Hinojos, W. Wang, N. Nijem, B. Shan, R. M. Wallace, K. Cho, Y. J. Chabal, *ACS Nano* 2012**, 6,** 5381.

[47] M. Farmanbar, G. Brocks, *Phys. Rev. B* 2016**, 93**, 085304.

[48] W. J. Yu, Y. Liu, H. Zhou, A. Yin, Z. Li, Y. Huang, X. Duan, Nat. Nanotechnol. 2013, **8**, 952.